Chapter 7
Surface Properties of Nanostructures Supported on Semiconductor Substrates

F. Krok, J. Konior, and M. Szymonski

Abstract The surface electronic properties, related to nanostructures grown on semiconductor substrates, are presented. Major experimental results were obtained in UHV with the use of Kelvin probe force microscopy (KPFM). Investigated systems include epitaxial nanostructures assembled on InSb(0 0 1) by submonolayer deposition of Au, semiconductor nanostructures grown on lattice-mismatched semiconductor substrates, semiconductor surfaces with surface modification and nanostructuring induced by ionizing irradiation, and dielectric structures grown on InSb(0 0 1). A new efficient algorithm for the evaluation of electrostatic forces in the tip–plane system is also presented. As a theoretical step, the results of contact potential difference values for tip–plane systems are presented and compared with the experimental data, showing good agreement between theory and experiment. We also analyze and discuss the important issue of high resolution contrast obtained, with the use of the KPFM method. In particular, using the Au/InSb(0 0 1) system as an example, we address a key problem of the limits of lateral resolution in KPFM. Then, the subject of the quasi-spectroscopic KPFM measurements is being discussed, together with the phenomenon of the so-called short-range bias-dependent electrostatic interactions.

7.1 Introduction

In the advent of nanotechnology, the growth of nanostructures on substrate surfaces has been extensively studied driven by the interest in new physical and chemical properties of structures of reduced dimensions. A recent tendency in miniaturization of electronic devices, as well as exciting prospects of new emerging technologies are

F. Krok (✉) · J. Konior, · M. Szymonski
Institute of Physics, Jagiellonian University, ul. Reymonta 4, 30-059 Krakow, Poland
e-mail: franciszek.krok@uj.edu.pl

S. Sadewasser and T. Glatzel (eds.), *Kelvin Probe Force Microscopy*, Springer Series in Surface Sciences 48, DOI 10.1007/978-3-642-22566-6_7,
© Springer-Verlag Berlin Heidelberg 2012

prompting a huge interest in the science of nanostructured materials. In particular, there is a need to develop efficient methods for preparation of functionalized surfaces with desired structural and electronic properties. Standard spectroscopic techniques used for the surface characterization, like for example, determination of surface voltage, surface barrier height, interface trap density or doping density, are insufficient when applied to the characterization of nanometer size objects due to their limited spatial resolution. Particularly, the measurement of the nanometer-scale surface potential distribution is necessary for analyzing nanodevice properties. Therefore, there is a need for developing nondestructive, diagnostic tools that can probe into a variety of surface related properties, down to a nanometer scale range. In this chapter we demonstrate that the Kelvin probe force microscopy (KPFM) technique can be used for the characterization of nanosized structures deposited on semiconductor surfaces. The KPFM technique, based on dynamic force microscopy (DFM) principles, gives information on topography and potential distribution of the sample with high spatial resolution.

The chapter is organized as follows. In Sect. 7.2, the KPFM experimental system is described together with the optimization procedure of the feedback parameters for CPD measurements. In Sect. 7.3, the KPFM studies of surface properties of metallic and semiconductor nanostructures assembled on semiconductor substrates are shown. In Sect. 7.4, the results of KPFM imaging of the ion beam-induced nanostructuring of semiconductor surfaces are presented. Then, in Sect. 7.5, based on the example of dielectric films grown on InSb(0 0 1), we discuss the issue of ultimate sensitivity and lateral resolution of the KPFM technique. The experimental CPD contrasts are compared with predictions of the theoretical model (Sect. 7.5.2) of the tip–sample electrostatic interactions. In Sect. 7.6, using KPFM imaging of Au/InSb(0 0 1) as an example, we provide experimental evidence of KPFM sensitivity to short-range and bias-dependent interactions, acting between the tip and the surface. Finally, Sect. 7.7 summarizes the chapter.

7.2 Experimental

The essential part of the results presented in this chapter was obtained with a home-build KPFM, which is basically a modified VP2 AFM/STM Park Scientific Instruments (PSI) device. The KPFM measurements were performed in UHV (pressure $\sim 5 \times 10^{-11}$ mbar) and at room temperature (RT). Figure 7.1a presents a schematic plot of the VP2 STM/AFM set-up with the modification allowing for simultaneous contact potential difference (CPD) measurements (the electronics within the dashed line). In the measurements, the topography was acquired using a non-contact FM mode, with silicon (boron-doped) piezoresistive cantilevers, purchased from Park Scientific Instruments. Prior to the measurements the tip was cleaned in the UHV conditions following the procedure described in [1]. The tip of conical shape with a half opening angle of about 20°, has an apex radius of about 20 nm, as checked by high resolution scanning electron microscopy (SEM).

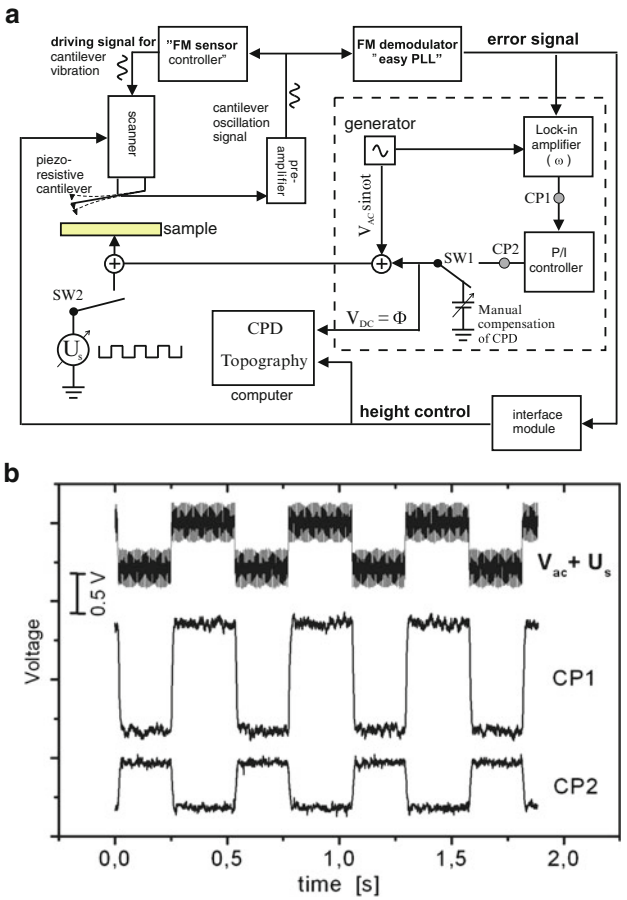

Fig. 7.1 (**a**) Schematic circuit diagram of the VP2 PSI setup with the modifications allowing for the operation in FM–KPFM mode in UHV (the scheme of electronics within the *dashed line*). (**b**) Signals which are tracked during the procedure of optimization of the electronic feedback parameters allowing for optimum performance of the CPD compensation. For fine tuning of the feedback, first the feedback loop is opened (SW1 set to manual) and an external square-wave voltage (SW2 – closed) is applied to the sample – see the upper signal ($V_{ac} + U_S$). Then, the lock-in parameters are optimized until the lock-in output signal (signal CP1) reflects the external square-wave voltage shape. Finally, with closed feedback loop (SW1 closed) the PI controller gains are optimized until its output signal (signal CP2) tracks the external voltage source

During the experiments, the frequency shift Δf with respect to the resonant frequency (detuning), was set in the range between −3 and −110 Hz, and a constant oscillation amplitude A was kept in the range between 20 and 50 nm; the scanning rate was 0.2–0.5 scanline per second. For the CPD measurements, the feedback electronics containing a sine-wave voltage generator, a lock-in amplifier (Stanford Research Systems, SR510) and PI controller was implemented to the original VP2

set-up. During the normal KPFM mode operation, the sample was biased with a *dc*-voltage plus an *ac*-voltage of angular frequency ω, with $f = \omega/2\pi = 600\,\text{Hz}$, and amplitude $V_{\text{ac}} = 300\,\text{mV}$. The time-dependent tip-sample interaction, with an angular frequency ω, induces a variation of the FM demodulator (Nanosurf "easyPLL") output. This ω-component is detected through the x-component of a lock-in amplifier, then a feedback loop (Kelvin PI controller) is used to add a *dc*-voltage to the sample in order to compensate the CPD between the tip and the sample. As a result, the acquired *dc*-map represents the distribution of the measured sample surface potential. By definition, throughout the chapter, the bright contrast on the CPD maps (the higher CPD) represents areas of a higher work function. In order to ensure the stable potential measurements and high sensitivity of the system, special care has been taken for proper optimization of the feedback parameters. In the electronics circuit, the access signal check points are added (see Fig. 7.1a) to control the output signals of the lock-in amplifier (CP1) and the PI controller (CP2). There are also two switches: SW1 to turn off the feedback for manual compensation of the CPD and SW2 to apply a square-wave voltage to the sample. In the following, we describe the procedure of optimization of the electronic feedback parameters, allowing for optimum performance of the CPD compensation. The procedure is performed upon the approach of the cantilever to the surface and before scanning the surface. First, with SW1, the circuit loop is opened and the *dc*-voltage is changed manually, until the CP1 signal becomes zero (the compensation of local CPD). Next, with the help of SW2, a square-wave voltage is supplied to the sample surface and the lock-in amplifier is tuned. The sensitivity, time constant, and phase shift of the lock-in amplifier are adjusted until the regular square-wave signal at CP1 is obtained. Then, for final tuning of the feedback with the help of SW1, the feedback loop is closed and the PI controller gains are optimized until the signal at CP2 tracks the external square-wave voltage. The signals are shown in Figure 7.1b. Once this is done, the external voltage is disconnected with SW2 and the system is ready to perform the measurements in the KPFM mode.

7.3 Self-Assembling on Semiconductor Surfaces

7.3.1 Epitaxial Au Nanostructures Assembled on InSb(0 0 1)

Metal nanostructures on surfaces are very often studied in view of their possible applications in various fields, including nanoelectronics. In particular, they could be essential for fabrication of atomic scale conductive interconnects providing electric contact with basic elements of molecular electronic devices, such as single organic molecules and molecular circuits [2]. From a practical perspective, semiconductors and insulators are the most interesting substrates, since their geometrical and electronic structures are well known and large atomically flat terraces of such materials can be prepared with sufficient precision. As a consequence, there is

an intense activity aiming to develop efficient methods for patterning on large scale substrates and films, with regular arrays of nanostructures having functional properties. Suitable solutions for such a task might be provided by thermally-assisted assembling processes occurring at atomically ordered surfaces of $A_{III}B_V$ semiconductors. In particular, gold seems to be a good candidate for manufacturing nanometer-scale flat metallic patches on surfaces and/or conductive nanowires, aligned by the strongly anisotropic structure of the surface reconstruction rows and ridges of the metal-terminated (0 0 1) face of $A_{III}B_V$ semiconductors [3]. In the case of submonolayer deposition of Au on reconstructed InSb(0 0 1), Goryl et al. [4] reported on formation, morphology, and composition of Au nanostructures strongly dependent on the substrate temperature during deposition, or post-growth thermal annealing. They have found that Au deposition on the substrate kept at 400 K results in the formation of rectangular islands with edges on average 15 nm long, oriented along $\langle 0\,1\,1 \rangle$ and $\langle 1\bar{1}0 \rangle$ crystallographic surface directions (see Fig. 7.2a). The

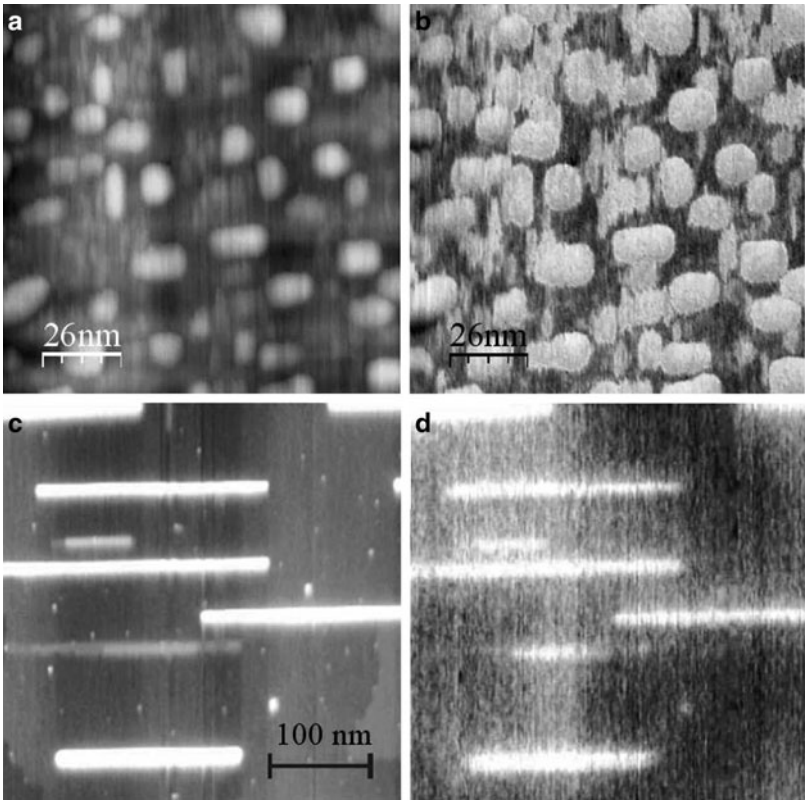

Fig. 7.2 Nanostructures created by Au deposition (<1 ML) on InSb(0 0 1) surfaces at temperatures of (**a**) 400 K and (**c**) 600 K with corresponding CPD maps (**b**) and (**d**), respectively. Sizes of the images: (**a**)–(**b**) 130×130 nm^2 and (**c**)–(**d**) 400×400 nm^2. Reproduced with permission from [3] and [4]

average height of the islands is of 1 nm. Although the reconstructed InSb(0 0 1)c (8×2) surface is strongly anisotropic and has the characteristic ridge-row structure along the ⟨110⟩ direction [5], there is no statistically significant preference in creating islands along atomic troughs on the InSb surface. This is consistent with previous reports, which state that large Au adsorbate clusters can disrupt the structure of the substrate and, therefore, they do not exhibit anisotropy along the ⟨1 1 0⟩ direction [6]. Also, the topography image shows that a certain amount of the deposited material is spread over the surface (between well defined islands), perhaps bound in the troughs of the reconstructed c(8×2) InSb(0 0 1) surface. A LEED pattern obtained for such a system indicates the c(8×2) reconstruction, characteristic for the clean substrate, although of somewhat lower quality, which might indicate that gold is not intermixing with the substrate material. Therefore, one could think that both the islands and the material accumulated between them are built of gold, not mixed with the substrate material. This hypothesis is confirmed by a CPD image presented in Figure 7.2b, showing a high quality contrast and a relatively low noise level. It is also evident that both the islands and the features between the islands have higher work function than the one corresponding to the substrate material. This is corroborated by the fact that the work function of Au(0 0 1) ($\phi = 5.2$ eV [7]) is higher than that of clean InSb(1 1 0) ($\phi = 4.7$ eV [8]).

For Au nanostructure assembling the substrate temperature seems to be the most important factor. A general tendency is that the higher the deposition temperature, the better organization of the nanostructures is observed. This is most likely due to the increase of gold atom diffusion with the temperature. Increasing the sample temperature during deposition by additional 200 K results in formation of narrow, long structures (nanowires) with a length up to 800 nm (see Fig. 7.2c). The nanowire orientation follows the ⟨110⟩ direction on the reconstructed InSb(0 0 1) surface. The nanowires are of different height and at both ends they have wings of lower height than the central part of the nanowires. The local CPD mapping of the nanostructures (Fig. 7.2d) exhibits a lack of contrast in the CPD signal over the wings and the nanowires with heights not exceeding two atomic layers. Only the nanowires with heights larger than 2 ML show an increased CPD with respect to the InSb(0 0 1) substrate surface. The KPFM measurements strongly indicate a non uniform chemical composition along the nanowires. The lack of the CPD contrast over the lower parts indicates that they are of the same chemical composition as the surrounding substrate surface. Accordingly, atomically resolved imaging of the wings (see Fig. 4 in [3]) closely resembles the structure of the substrate atomic reconstruction. The same behavior has been found for the nanowires with a height not exceeding 2 ML. Only the upper parts of the nanowires (>2 ML) have a regular 1×1 structure with the CPD clearly different from the substrate surface. Although this is a strong indication that the upper part of the nanowire is composed of gold atoms, recent STM measurements of nanowires assembled in a Au/InSb(0 0 1) system at 600 K do not support this expectation [9]. The STM images acquired with the chemical contrast on atomic-scale level have proven that the upper part of the nanowires is composed of two kinds of atomic species, most likely due to the formation of an InAu alloy phase. The height dependent composition of the

structures sheds light on the mechanism of self-organization of Au atoms on the InSb surface upon the deposition process [3].

Subsequent annealing of the system could produce further modification of its structure and atomic composition. It has been established that the post-growth annealing of the initial gold islands at a temperature of 600 K results in the formation of an InAu alloy phase [10]. Figure 7.3a, b presents the topography and the simultaneously acquired CPD map of the system of gold islands grown at 400 K and subsequently annealed to 600 K for 2 h. The islands preserved their initial rectangular shape, but their average size is almost doubled (16 nm across in comparison to 9 nm across as deposited) and the material accumulated previously in the substrate troughs, seen in Fig. 7.2a, disappeared. The corresponding CPD image, contrary to the KPFM measurements of the as-grown islands, shows significantly lower surface potential on the islands, as compared to the substrate. The inversion of the CPD contrast suggests a composition change of the islands. It seems that upon annealing in the presence of the gold overlayer there is a disruption of the cation–anion bonds on the substrate surface, leading to segregation of indium atoms

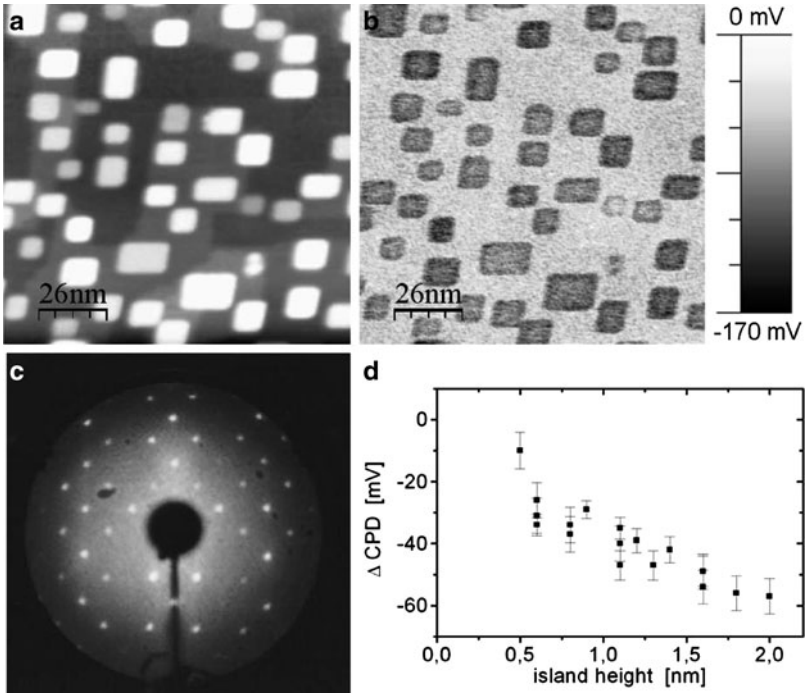

Fig. 7.3 (**a**) Topography and (**b**) CPD map of the Au/InSb(0 0 1) system grown at 400 K and later annealed to 650 K for 2 h. (**c**) Corresponding LEED image with the c(4×4) pattern characteristic for Sb-rich InSb surface reconstruction. (**d**) CPD signal dependence on the island height extracted from (**b**). The CPD gradually decreases with the island height and finally saturates at about −55 mV for the height of 2 nm. Reproduced with permission from [11]

and their dissolution in the Au islands [10]. Interdiffusion of surface In atoms into the islands should result in an enrichment of the substrate surface by Sb atoms. This hypothesis is supported by a LEED pattern of the annealed system (Fig. 7.3c) exhibiting the c(4×4) symmetry characteristic for a Sb-rich reconstruction. Since the islands cover less than 30% of the surface and the pattern is very bright, it is safe to assume that the LEED pattern comes predominantly from the substrate.

The surface potential of the islands depends on their height, as depicted in Figure 7.3d, in such a way that the higher islands exhibit lower CPD with respect to the substrate surface. The measured island surface potential monotonically decreases with the island height and finally saturates at the level of about −55 mV for an island height of about 2 nm. Such a dependence of the metal overlayer work function on the overlayer thickness, with its subsequent saturation at some level, is commonly observed. For example, in the Au/W(0 0 1) system [12], the measured work function saturates at a value corresponding to the one of bulk Au, at the minimum coverage of 3 ML of Au. Moreover, the high-resolution KPFM imaging of the islands shows that the work function is not uniform across the island and it is lower on the island edges than in its central part. A laterally resolved CPD measurement on a single island step is shown in Fig. 7.4b. As expected, the CPD signal along the island edge is reduced with respect to the island top surface. From the ΔCPD histogram (Fig. 7.4c), the relative decrease of the CPD at the edge is about 11 mV. It is well known from macroscopic contact potential (CP) investigations that stepped metal surfaces exhibit a lower work function when compared to flat surfaces [13], which can be simply explained in the frame of the jellium model approximation [14]. It is known that a considerable smoothing of the electron density occurs at stepped metal surfaces [15] due to the fact that the energy of an electron in the vicinity of a large flat plane is lower than when it is surrounded by complicated morphologies like, for example, a step edge. This means that charge flows from hills into the valleys formed by the surface atoms of the step edge (see Fig. 7.4d). Consequently, on the hill a net positive charge arises whereas at the valley there is a net negative charge inducing the dipole moments at the steps and finally, the decrease of the work function.

7.3.2 Semiconductor Nanostructures Grown on Lattice-Mismatched Semiconductor Substrates

Due to its unique capabilities, KPFM is often used for the characterization of self-assembled semiconductor nanostructures [like quantum wires (QWrs) and dots (QDs)] grown on lattice-mismatched semiconductor substrates. Such nanostructures are widely studied not only for better understanding of low-dimensional electron systems [16] but also due to important applications in electronic and photonic design and manufacturing [17, 18]. Further interest in studying nanometer-size QDs stems from their extraordinary abilities for charge storage [19], cold electron

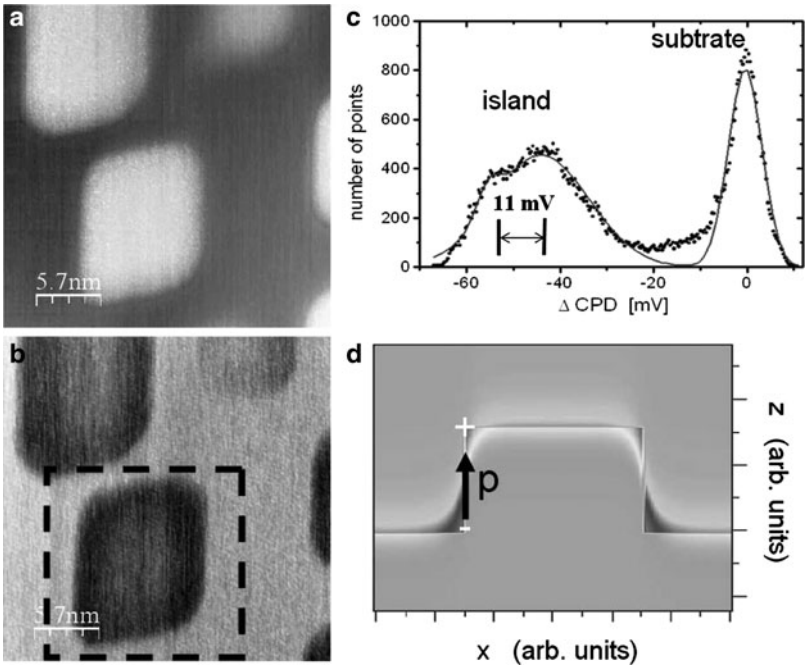

Fig. 7.4 (**a**) High-resolution topography image of the Au/InSb(001) system after annealing to 650 K with (**b**) corresponding CPD map. The measured CPD signal is not uniform across the whole island. (**c**) CPD histogram taken over the marked area in (**b**). The contact potential on the island edge is about 11 mV lower compared to the top of the island as can be seen from the histogram. (**d**) The decrease of the CPD signal at the edge is attributed to the dipole moments which are localized at the step in the frame of the jellium model approximation for stepped metal surfaces. The drawing in (**d**) is from [14]

emission [20], and photoluminescence [21]. The work function of a single QD is an important parameter for such a device because it is related to the barrier height for the carrier injection into, or for the carrier ejection from the QD. The KPFM is a powerful tool for investigation of the local electronic states and transport properties of modern nanoelectronic devices. Salem et al. [22] used the KPFM, under ambient conditions, to investigate the CPD of nanocrystalline silicon (nc-Si) dots with various sizes before and after dot charging. nc-Si dots of 2–8 nm were grown by plasma decomposition of SiH_4 on a thin SiO_2 layer, covering the Si(100) substrate surface. The local charge injection to the dots was performed using the biased tip in the contact mode. Figure 7.5 shows the topography and CPD images of the nc-Si dots as-grown ((a) and (b)) and after the charging process ((c) and (d)), respectively. It is seen that the charging process does not change the substrate surface potential, whereas it influences the local surface potential of the dots. The change of the dot CPD depends on the dot size, i.e., larger dots have a higher potential value. These experimental findings indicate that the KPFM allows for detection of the quantity

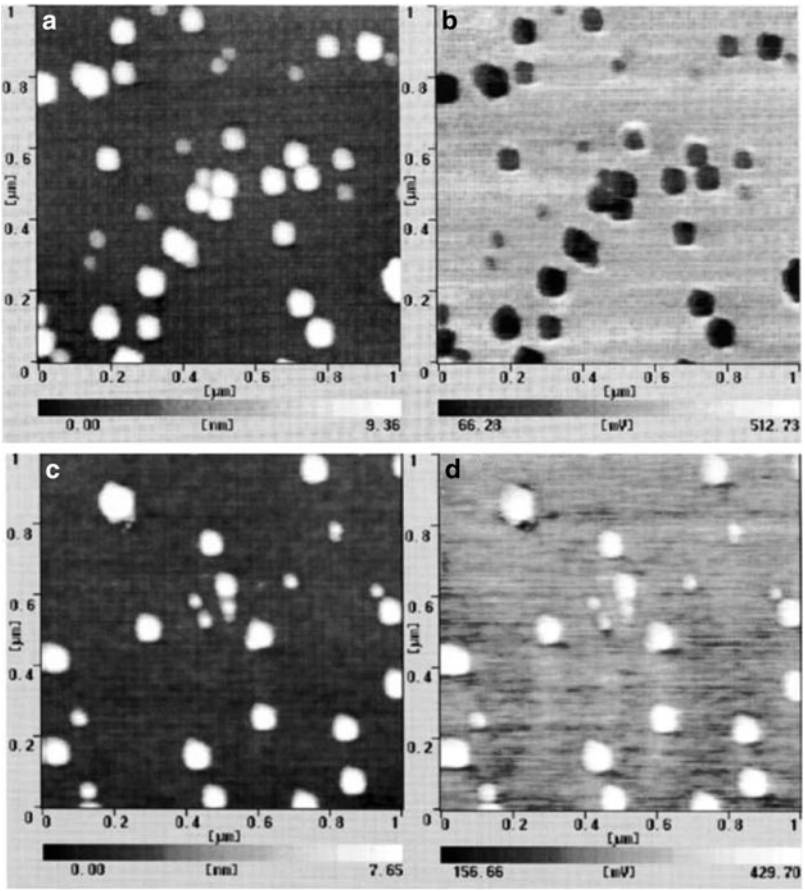

Fig. 7.5 (**a**) Topographic and (**b**) corresponding surface potential images for nc-Si dots before and (**c**) and (**d**) after dots charging, respectively (Reprinted with permission from [22]. Copyright 2007, American Institute of Physics)

of the charge confined in nanostructured objects. Measuring the CPD changes as a function of the dot diameter and comparing the results with the calculated charging energy of separated dots, the number of injected electrons can be evaluated. It has been found [22] that one electron could be stored in a nc-Si dot of diameter up to 2.8 nm, whereas there can be three electrons in dots having diameters from 4.7 to 7.4 nm.

Yamauchi et al. [23] used KPFM in UHV to investigate the correlation between the size and the local work function of InAs QDs, grown on GaAs(0 0 1). The QDs of height from 1.3 to 7.2 nm and lateral size from 20 to 40 nm have been grown by molecular beam epitaxy (MBE). The measured values of the InAs QDs CPD depend on the dot height, as shown in Figure 7.6. The height dependence of the

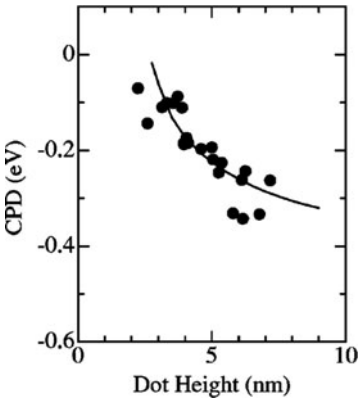

Fig. 7.6 Dot height dependence of the CPD for InAs QDs. *Closed circles* and the *solid curve* indicate the measured CPD and the calculated one, respectively. The numerical calculations of the dot height dependence of the surface potential were performed taking into account a quantum disk model for the quantum size effect [24]. The presented CPD is expressed in values relative to the wetting layer (WL) value (Reprinted with permission from [23]. Copyright 2007, American Institute of Physics)

CPD is interpreted in terms of the quantum size effects, by which the amount of charge accumulated in the QD is determined by the discrete energy levels of the QD. That is, in thermodynamic equilibrium, due to the difference of the Fermi energies of InAs and GaAs, the carriers (mostly electrons) in the InAs/GaAs heterostructure should be transferred from a GaAs to an InAs dot. Then, the charge distribution induced by the charge transfer creates an electrostatic potential on the QD surface. Carriers in the InAs QD are confined in the nanometer-scale region and the discrete energy levels are created. The net number of carriers transferred into the InAs dots depends on the energy difference between the discrete levels in the dot and the conduction-band bottom of the substrate. Therefore, the local surface potential of the QDs created by the charge distribution depends on the dot height through the number of discrete energy levels.

7.4 Surface Modification and Nanostructuring Induced by Laser Ablation and Ion Beams

Apart from self-assembling of the deposited material presented in the previous sections, there is another convenient technique for surface nano-manufacturing. For decades, it has been known that the interaction of particles and photons with solids leads to modification of their surfaces and formation of regular, periodic nanostructure patterns like ripples, dots, or wires [25, 26]. It appears that the

particular shape and size of such structures can be controlled by a proper choice of the irradiation conditions [27, 28].

In the case of laser-induced ablation, the ripple or dot patterns result from non uniform melting, due to intensity variations in the interference pattern between the incident laser field and the surface or capillary wave of same frequency, induced in the target [29]. Reif et al. [30] reported the use of KPFM to study the electronic properties of a nanostructured silicon surface produced by femtosecond laser ablation. Figure 7.7a presents the chains of regularly arranged spherical nanodots with a diameter of about 120 nm produced on silicon surface at an intermediate dose (1,000 pulses at 1.1×10^{12} W cm^{-2}). Such a morphology is of interest for possible applications as a template for biomolecule immobilization. Although the target is composed of a single element material, the KPFM measurements revealed a variation of the surface potential of the nanostructured Si surface, as it is shown in Fig. 7.7b, where the CPD of the laser-induced nanodots is decreased by about 50 mV with respect to the untreated substrate. It is proposed that the CPD map reflects the local change of the sample contact potential, since experiments on similar structures on metalized dielectrics showed that purely topological variations alone could not result in a variation of the CPD signal. In order to explain the origin of the observed contrast in the CPD of laser ablated silicon, the dependence of the CPD signal variation on the dopant concentration of the irradiated silicon crystals has been measured. The obtained results indicate that a dopant segregation due to partial liquefaction is the main mechanism responsible for the change of the surface potential on the laser ablated silicon surfaces [30].

In the case of ion bombarded solids, the main processes involved in nanostructuring are: surface sputtering, mass transport processes due to momentum transfer

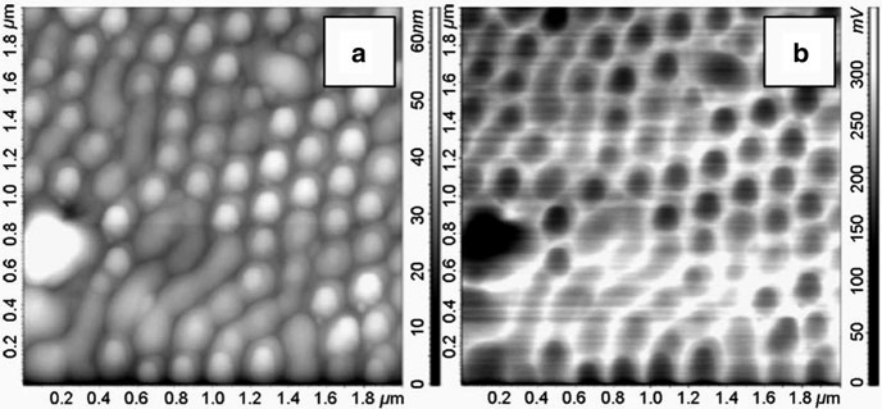

Fig. 7.7 (**a**) Typical morphology of femtosecond laser ablated silicon (a circular laser polarization) exhibiting chains of spherical nanodots with a diameter of about 120 nm and (**b**) the simultaneously recorded CPD map. The surface potential of the nanodots is lower by about 50 mV as compared to the one of the surrounding area. The measurement was performed at ambient conditions. Reproduced with permission from [30]

in the collision cascades in the target, and diffusion (thermally or beam enhanced) on the irradiated surfaces. Typically, for the normal ion beam incidence dot patterns are observed [31], whereas for the oblique incidence periodic height modulations (ripple structures) are observed [32]. The above behavior is also seen for the InSb(0 0 1) surface where dot-like and wire-like structures of diameter of a few tens of nanometers are created [33]. Apart from the morphological evolution, ion bombardment can also induce changes in the elemental composition of irradiated multi-component surfaces. Due to preferential sputtering, partial sputtering yields depend on the atomic masses and surface binding energies of the constituents [34]. Such theoretical predictions are consistent with an experimentally observed large non-stoichiometry for the InP surface [35], possibly because of the large mass difference between In and P atoms. However, for compounds with similar masses of the constituents, like GaAs or InSb, this theory is not able to predict partial sputtering yield ratios.

KPFM can provide valuable information on the composition of ion-induced nanostructures on InSb(0 0 1). In Figure 7.8, the topography and the CPD images of a InSb(0 0 1) surface irradiated with an Ar ion beam at 4 keV and a fluence of 2.1×10^{16} ions/cm^2, are shown. In the topography image (Fig. 7.8a), there are two dots interconnected with a long wire. There is also a small cluster close to the wire. In the CPD image (Fig. 7.8b), the corresponding CPD signal contrast indicates that all those structures are made of a material with a different work function with respect to the surrounding InSb substrate. For both, the wire and the dots, the work function is lower than for the substrate area. The decrease of the work function is size dependent, as illustrated by the line profile across the surface contact potential image (Fig. 7.8c). The potential of the larger dot is lower by about 50 mV with respect

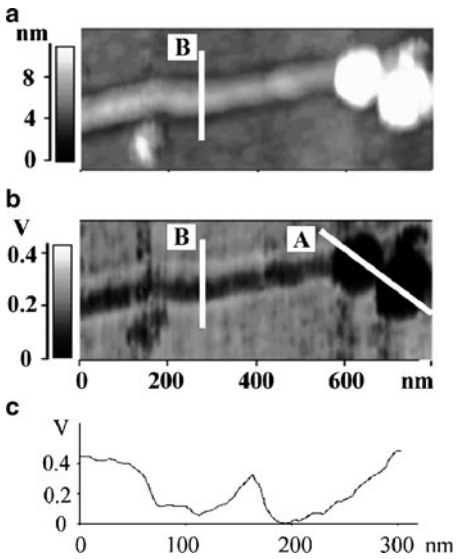

Fig. 7.8 (**a**) Topography and (**b**) CPD images of nanostructures developed on a InSb(0 01) surface irradiated with a 4 keV Ar ion beam and acquired with KPFM. (**c**) Line profile of the CPD map of the dots, taken along the line marked by A. From [33]

to the potential of the neighboring smaller dot. The CPD contrast of the wire, on average, is less than half of the dots (Figs. 7.8c and 7.9). However, the differences in CPD values cannot be directly ascribed to the differences in the relative composition of In and Sb in the nanostructures. The electrostatic force is a long-range interaction and, as a result, the obtained surface potential distribution can also be affected by averaging effects due to a finite tip size. Results of several other experiments, in which ion irradiated InSb surfaces were investigated with spectroscopic methods indicate that the surfaces are enriched in indium [36]. However, a lack of the lateral resolution in the spectroscopic measurements does not allow for a direct determination of the form in which the excess indium atoms are accumulated on the bombarded surface. We have compared these results with the KPFM measurements performed on the nanostructured InSb(0 0 1) surface. KPFM could reveal that the wires and the dots are made of a material with a different work function than that for the irradiated InSb (see Fig. 7.8b). The lower work function of the nanostructures compared with that of the substrate, indicates the excess of indium, since the work function of In ($\phi_{\mathrm{In}} = 4.12\,\mathrm{eV}$) is lower than that of the irradiated InSb(0 0 1) surface ($\phi_{\mathrm{irrad.InSb}} = 4.6\,\mathrm{eV}$ [37]).

Indium enrichment of the wires and dots means that there are metallic-type structures generated on the semiconductor substrate [38]. In such a case, the condition of thermodynamic equilibrium implies that the Fermi levels of the two materials must coincide with each other. This condition is fulfilled due to a charge transfer and band bending near the interface in analogy with that on the interface between a bulk metal and a semiconductor (Schottky barrier model). The direction of electron flux in a metal–semiconductor contact depends upon the relative values of work functions of the two materials and the electrons will travel from the material with the smaller work function to the material with the higher one. As in the present

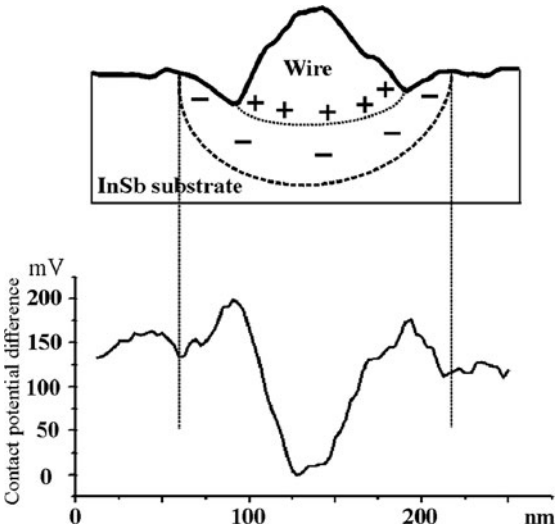

Fig. 7.9 Line profiles of the wire topography (*upper graph*) with the corresponding profile of the CPD signal (*lower graph*). The profiles are taken along the lines marked with B in Figure 7.8a, b, respectively. In the upper graph a substrate region enriched in electrons is drawn schematically. From [33]

case, $\phi_{\text{nanostructure}} < \phi_{\text{substrate}}$, the electrons are transferred from the nanostructures to the substrate. As a result, the metal–semiconductor interface is charged and there is a certain region in the semiconductor substrate enriched in electrons. Figure 7.9 shows the line profile (cross-section) of the wire (taken along line B in Fig. 7.8), with the corresponding cross-section of the wire's CPD image. The deep minimum in the CPD signal, corresponding to the potential of the wire, is accompanied by two "shoulders" on its both sides. The signal at the shoulder maxima is higher by about 50 mV in comparison with the potential of the InSb substrate. In the CPD image (Fig. 7.8b) the "shoulders" are visible as two bright stripes, aligned along the broad dark stripe, corresponding to the CPD of the wire. The maximum of the "shoulders" corresponds to the border between the wire and the substrate. It is likely that the increased CPD signal in the shoulders reflects the charged metal-semiconductor interface. We have associated the width of the CPD "shoulders" (from their onset to their maximum) with the thickness of the substrate region enriched in electrons. In Figure 7.9, a cross-section of the substrate region enriched in electrons is drawn schematically. The termination of the enriched region on the surface implies that the substrate areas on both sides of the wire should be negatively charged. In fact, the increased magnitude of the CPD signals on both sides of the wire support the concept that the areas around the wire are negatively charged. This was already shown by Sommerhalter et al. [39], who demonstrated that in the CPD image the bright contrast corresponds to negatively charged areas.

7.5 Dielectric Structures Grown on InSb(0 0 1)

Apart from metallic and semiconductor nanostructures on surfaces, the KPFM technique has been also used to study the properties of insulating films on semiconductor surfaces. In particular, alkali halide films are often considered as model systems and they have been studied extensively in recent years. This is both, because of their interesting physical properties and because of their importance as insulator/semiconductor interfaces in all technologies for electronics. It has been established that alkali halide films can be grown epitaxially on $A_{III}B_V$ compound semiconductors [40]. This is due to a strong chemical bond between the halogen ion and the A_{III} atom on the substrate surface, and due to the possibility of choosing the $A_{III}B_V$ compound with a lattice (zincblende type) matched closely to the lattice of the given alkali halide (rock-salt type). An example of a closely matched alkali halide/$A_{III}B_V$ adsorption system is KBr/InSb(0 0 1): InSb has the lattice constant 6.47 Å and KBr has the lattice constant 6.58 Å.

A typical topographical image of the KBr/InSb(0 0 1) surface is shown in Figure 7.10a. The coverage of KBr is about 0.2 ML. The substrate surface is composed of large, atomically flat terraces. The monatomic substrate steps are oriented along the main substrate surface crystallographic directions of $\langle 1\,1\,0\rangle$ and $\langle 1\bar{1}0\rangle$.

KBr is aggregated into monoatomically thick islands (visible on the image as brighter features) which are elongated along the $\langle 1\,1\,0\rangle$ crystallographic direction.

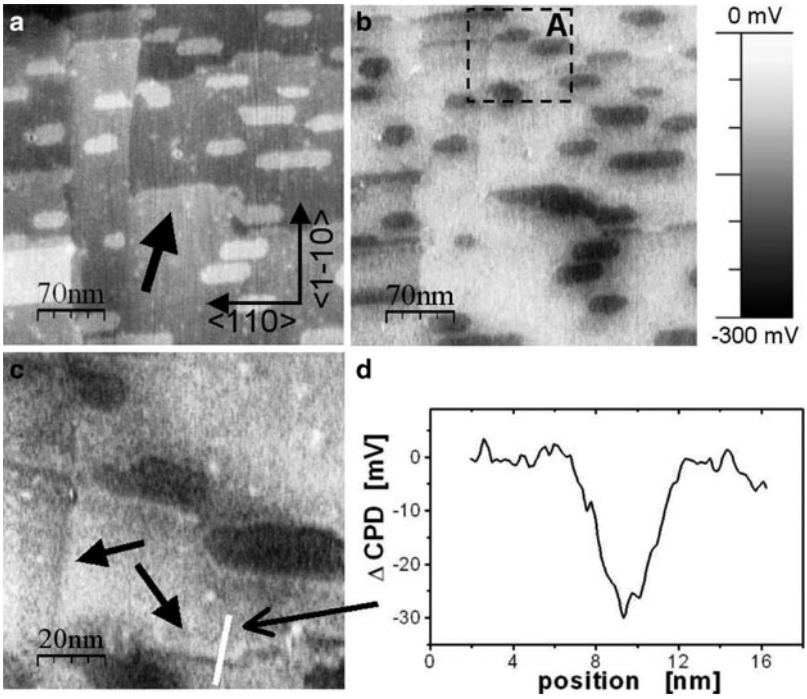

Fig. 7.10 (**a**) Topography and (**b**) CPD images of KBr islands grown on a InSb(0 0 1) surface acquired with KPFM. The *black arrow* in (**a**) indicates the KBr island which is topographically not resolved from the substrate terrace and can be identified only with the help of the CPD image. (**c**) High-resolution CPD image of the zone marked with A in (**b**). Together with the decreased CPD signal corresponding to the KBr islands, a dark zigzag line (indicated by the *black arrows*) corresponding to the substrate terrace edges and reflecting the variation of electrostatic potential along the substrate monatomic steps is observed. (**d**) Line profile of the CPD taken along the white line indicated in (**c**). From [41]

The island shapes indicate that the diffusion of KBr molecules during the film growth is highly anisotropic; this is due to the structure of the substrate surface, which is composed of atomic rows along the ⟨1 1 0⟩ direction [5]. The KBr molecules aggregate into compact islands of different lateral size but uniform in height (i.e., of 1ML thickness). The average lateral dimensions of islands can be controlled by the amount of deposited material, i.e., the surface coverage. Depending on the nominal surface coverage of KBr, islands as small as a few nm^2 and as large as $100 \times 100\,nm^2$ can be created, with the coverage in the range from 0.2 to 0.7 ML of KBr, respectively.

A CPD image of the KBr/InSb(0 0 1) surface, acquired simultaneously with the surface topography is shown in Figure 7.10b. The dark features on the CPD map correspond to the KBr islands. The darker contrast on the KBr islands (lower voltage) corresponds to a locally decreased work function of the islands,

as compared to the substrate. There are a few features of the system under study which are discussed below.

First, there is a straightforward observation, emerging from the comparison of Figure 7.10a, b, which demonstrates the advantage of using KPFM for imaging heterogeneous surfaces. That is, there are some KBr islands (marked by the arrow in Fig. 7.10a), which have grown up attached to the substrate terrace edge and they are topographically not distinguishable from the substrate terrace. They can be recognized only if the CPD signal is acquired simultaneously with the topography.

Second, by compensating the electrostatic interaction, KPFM can image the true topography of heterogeneous structures, contrary to what is measured with the conventional dynamic force microscopy (DFM) technique [42]. For DFM, the surface topography is acquired by keeping the total interaction between the vibrating cantilever and the sample constant. In the case of imaging heterogeneous structures, the visible topography is highly influenced by the difference of the electrostatic interaction between the probe and the imaged surface areas of different composition. For the KBr/InSb the "height" of the KBr islands measured in the DFM images (the sample bias kept constant) is about 2.57 Å, whereas KPFM reads a "height" of about 3.19 Å. The last value is in good agreement with the height of a monatomic terrace step on the KBr(0 0 1) crystal surface ($\sim$ 3.32 Å) as measured with DFM alone.

Third, the high-resolution CPD map presented in Figure 7.10c reveals that the two KBr islands, separated by 4 nm from each other, can easily be distinguished. Moreover, in the CPD map seen in Figure 7.10c, together with the "dark islands" corresponding to the KBr overlayers, there is a decrease of the surface potential visible in a form of a zigzag line (see the black arrows in the image). The zigzag line corresponds to the substrate terrace edges and it reflects the variation of the electrostatic potential (ES) across the monatomic steps. The variation of the ES indicates trapping of electrical charge at step states which induces pinning of the Fermi level [39]. The measured drop of the CPD (decrease of the work function) indicates that the steps are positively charged. In Figure 7.10d the cross section of the CPD values, taken along the white line indicated in Figure 7.10c, shows a drop in the CPD signal of about 30 mV. However, the measured value of the reduction of the surface potential should not be directly assigned to the magnitude of a variation of the electrostatic potential. Most likely the true local ES variation is much higher but the measured value is highly influenced by averaging due to the large tip size. This can be also deduced from the line profile, the spatial resolution in the KPFM measurements is of 5 nm.

7.5.1 Accuracy of KPFM Signal Measurements

There is yet another issue we would like to point out on the example of KPFM imaging of the KBr/InSb(0 0 1) system. That is, in the CPD images shown in Figure 7.10b ,c, the shapes of the KBr islands are well defined, although the surface potential on the substrate and the island sites is not homogeneous. The

inhomogeneity of the surface potential results from the influence of the averaging effect on the measured CPD values, due to the finite tip size. The CPD signal gets lowered when measured close to or between the islands. The non-uniformity of the substrate work function points out to the issue of the accuracy of CPD signal measurements. There are two effects that may influence the correctness of CPD measurements and they should be considered as stemming from the long-range nature of the electrostatic forces. First, the averaging of the measured CPD is due to the contribution of the whole tip, which is much larger than the island itself. Thus, the region surrounding the island contributes to the measured CPD values. Second, the tip vibrations make the obtained CPD values averaged over the whole tip trajectory.

To determine the relative change of the KBr island work function with respect to the substrate surface work function, we first employ the point Kelvin probe force spectroscopy (KPFS). In Figure 7.11 the Kelvin probe force spectroscopy performed on the InSb(0 0 1) surface covered with a submonolayer of KBr film is shown. To perform the KPFS measurements, at first, the surface is imaged to obtain the topography. Subsequently, the scan range is set to zero and the probe is moved to the desired location (over the substrate surface to point A) for the KPFS. Then, the feedback loop is disabled and the sample bias is scanned over a certain range. Simultaneously, the error signal (detuning) from the PLL demodulator is collected. Since the tip–sample distance is kept constant during the KPFS measurements (disabled feedback loop), the detuning signal versus bias voltage curve is characteristic of a pure electrostatic force in the tip–sample system. Subsequently, the measurement is repeated over the KBr island [point (B)]. In both cases a parabolic dependence of the detuning signal on the bias voltage is obtained since the electrostatic force is a quadratic function of the bias voltage (see Fig. 7.11b). The maxima correspond to the sample bias, for which the CPD between the chosen areas on the surface and the tip is nullified. Although the absolute values of the tip work function is unknown, the difference in the surface potentials of the two different locations on the sample surface can be measured. The relative difference of the sample bias voltage, corresponding to the parabola maximum,

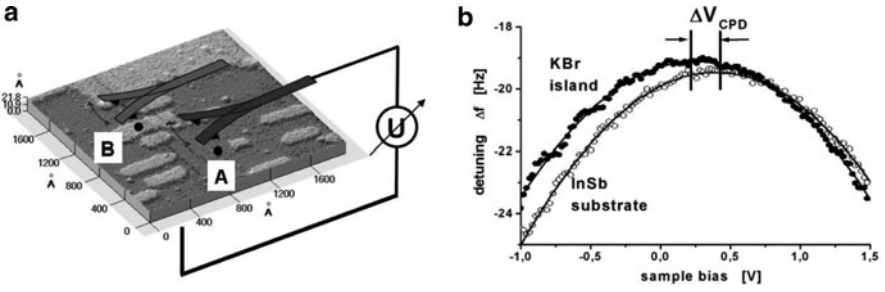

Fig. 7.11 Principle of the Kelvin probe force spectroscopy performed on the KBr/InSb(001) system. In (**a**) the topography of the KBr/InSb surface with the two points marked with A (substrate) and B (KBr island) where the dependence of detuning versus sample bias voltage were taken and are presented in (**b**). From [43]

provides the difference in the contact potentials of the surface sites, where the spectroscopy is performed. The KPFS measurements prove that the work function of the KBr film (or the KBr/InSb interface) is lower by about 210 meV with respect to the work function of the bare and clean InSb surface.

A wide range of KBr island sizes, grown on InSb, offers great opportunities for studying the lateral resolution, as well as for checking the accuracy of the KPFM contrast. For studying the limits of the CPD signal accuracy in FM–KPFM measurements, we have analyzed the dependence of CPD, as taken over the KBr islands, on lateral island dimensions. We selected the islands with the length to width ratio not higher than 1.5 and then we assumed the islands to be of equivalent quadratic shape. In Figure 7.12, the measured CPD, as a function of the KBr island size (i.e., the island side length), is shown. It is clear that the measured CPD depends on the size of the islands and CPD saturates for the island size larger than 100 nm.

The value of the saturated CPD in FM–KPFM corresponds to the values measured with point KPFS and indicates that there is no observable tip-induced band bending effect for the system under study, as demonstrated recently by Rosenwaks et al. [44]. We have found that the observed saturation of the CPD for islands of size around 100 nm is in good agreement with the previously reported lateral resolution of FM–KPFM of 50 nm, obtained by Zerweck et al. [45], when only a single boundary of a KCl island grown on Au was imaged. When even smaller KBr islands are imaged, the tip obviously also senses the contact potential of the substrate and hence the CPD is significantly reduced. According to the experimental data, when the size of the KBr islands is comparable to the size of the tip apex (i.e., about 20 nm) the CPD signal provides only about 50% of the correct potential value (see Fig. 7.12).

7.5.2 Theoretical Model of Electrostatic Tip–Sample Interaction

In order to analyze and understand the KPFM experimental results, the electrostatic forces in tip–plane systems have to be evaluated with sufficient accuracy and reasonable computing effort. The main difficulty in such a computation is due to

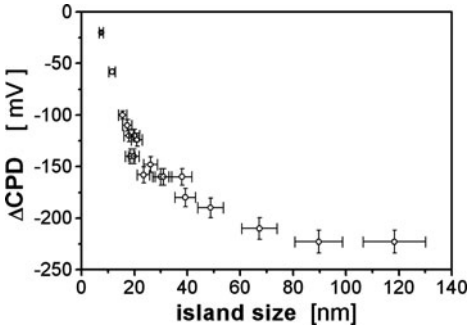

Fig. 7.12 Measured CPD over the KBr islands versus the island size. The evaluated tip–sample distance is of 1 nm

the large variation of the geometrical scale, as the tip–plane distance, tip size, and the plane dimension differ in orders of magnitude. Also, non-constant potential distributions on a plane – which are due to differences in the work function of various materials placed onto the plane – may introduce further difficulties. In the simplest case, considered in most of the theoretical investigations, the plane has a fixed electrostatic potential relative to an axially symmetric tip placed above the plane. Except for the simple cases of high symmetry tips, such as a sphere [46], analytical solutions for such problems are not usually possible. As a result, almost all important results were obtained by various numerical [47–52] or quasi-analytical [45,53,54] methods. In [55], we have presented an efficient method for calculating the electrostatic force in tip–plane systems. The method is suitable for an arbitrary surface potential distribution and it consists of two basic steps. First, the Green function formalism is applied to integrate out exactly the potential distribution in the plane, reducing the task to an effective electrostatic boundary value problem for the tip surface only.

In the second step, the resulting effective problem is solved by a standard numerical scheme. It should be stressed that on the contrary to many previously published methods [45, 47–54], the developed approach is not limited to a constant value of the plane potential and, furthermore, does not require the tip to be axially symmetric.

To analyze the effect of experimental conditions on the accuracy of FM–KPFM results, we calculated numerically the CPD values for an idealistic tip–surface geometry and for non-uniform potential distributions on the surface. As the first step of the calculation, an electrostatic tip–surface force was evaluated with an efficient method suitable for an arbitrary surface potential distribution. In the following part of this subsection, the essential elements of the developed method [55] and calculated results are presented.

7.5.2.1 Outline of the Method

The system considered is built of an infinite plane surface, at $z = 0$, and the tip placed in the region $z > 0$. The approximation to an infinite plane seems sufficient for most applications, where the plane segment is much larger than the tip size and the tip–surface distance. The electrostatic potential distribution in the plane is denoted by $V_1(x, y)$ and the potential of the tip surface is fixed at V_0. The above described original electrostatic potential problem is known in electrostatics as the Dirichlet boundary value problem and it was shown in [55], finding the tip surface charge density $\sigma(\mathbf{r})$ is equivalent to solving the following linear integral equation:

$$V_0 = \Phi_1(\mathbf{r}) + \frac{1}{4\pi\epsilon_0} \oint_{TS} G(\mathbf{r}, \mathbf{r}')\sigma(\mathbf{r}')\, \mathrm{d}S', \tag{7.1}$$

with the unknown surface charge density function $\sigma(\mathbf{r})$ being limited to only the tip–surface ($\mathbf{r} \in TS$). The physical meaning of (7.1) is the following. The electrostatic

potential on the tip–surface, being equal V_0, has two sources: the plane potential distribution $V_1(x, y)$ and the tip surface charge density $\sigma(\mathbf{r})$. The function $\Phi_1(\mathbf{r})$ includes all the contribution from the plane and is given by the following surface integral involving $V_1(x, y)$ and the outward normal derivative of the electrostatic Green function $G(\mathbf{r}, \mathbf{r}')$:

$$\begin{aligned}\Phi_1(\mathbf{r}) &\stackrel{\text{def}}{=} -\frac{1}{4\pi}\oint_{z'=0}\frac{\partial G(\mathbf{r},\mathbf{r}')}{\partial n'}V_1(x',y')\,\mathrm{d}x'\,\mathrm{d}y' \\ &= +\frac{1}{4\pi}\oint_{z'=0}\frac{\partial G(\mathbf{r},\mathbf{r}')}{\partial z'}V_1(x',y')\,\mathrm{d}x'\,\mathrm{d}y'. \end{aligned} \tag{7.2}$$

Here $G(\mathbf{r}, \mathbf{r}')$ is the exact electrostatic Green function [56]:

$$G(\mathbf{r},\mathbf{r}') = \frac{1}{|\mathbf{r}-\mathbf{r}'|} - \frac{1}{|\mathbf{r}-\mathbf{r}'_1|}, \tag{7.3}$$

with the vectors $\mathbf{r} = [x, y, z]$, $\mathbf{r}' = [x', y', z']$, and $\mathbf{r}'_1 = [x', y', -z']$. The integral term of the right side in (7.1) is the tip surface charge density contribution to the electrostatic potential on the tip surface. It is composed of two subterms, one follows from the Coulomb law, while the second presents the image charge contribution [therefore, there are two terms present in (7.3)]. Equation (7.1) is exactly equivalent to the original problem formulated for the plane plus tip surface system with an arbitrary potential distribution on the plane. Moreover, as we proved in [55], for any rectangle type region in the plane, the integral in (7.2) may be evaluated analytically.

7.5.2.2 Numerical Implementation

After the plane contribution to the potential is integrated out exactly and the term $\Phi_1(\mathbf{r})$ is evaluated, any of the existing numerical methods may be used to solve the resulting integral equation. The method we used is similar to the so-called surface charge method [50] and with this method, calculation of the force on the tip proceeds as follows. The tip surface is first divided into N small surface segments ΔS_i, each with the central point at $\mathbf{r}_i$ and with constant surface charge density σ_i. Then, using (7.1) for these points, the following set of N linear equations is obtained:

$$V_0 - \Phi_1(\mathbf{r}_j) = \sum_{i=1}^{N} F_{ji}\sigma_i, \tag{7.4}$$

with the free term contribution $\Phi_1(\mathbf{r}_j)$ computed from (7.2) and $j = 1, 2, \ldots, N$. The matrix elements F_{ji} are defined as:

$$F_{ji} = \frac{1}{4\pi\epsilon_0}\oint_{\Delta S_i} G(\mathbf{r}_j,\mathbf{r}')\,\mathrm{d}S', \tag{7.5}$$

and for a given tip–plane geometry, the elements F_{ji} are evaluated and stored for subsequent use. The system of linear equations (7.4) is the main formula for the numerical implementation of the method and shows explicitly its advantage by limiting computation to the finite tip surface, thus eliminating from the numerical part of the infinite plane. Once the system of N linear equations (7.4) is numerically solved, the surface charge densities σ_i are known and the force acting on the tip may be evaluated:

$$\mathbf{F} = \frac{1}{2\epsilon_0} \sum_{i=1}^{N} \sigma_i^2 \Delta S_i \hat{\mathbf{n}}_i , \tag{7.6}$$

with $\hat{\mathbf{n}}_i$ being the unit vector normal to the tip surface at $\mathbf{r}_i$.

7.5.2.3 Main Calculated Results

To test the proposed method, a system with typical and realistic geometry was investigated. Figure 7.13 shows geometrical details of the system studied, in which the tip consists of a cone with spherical end segments. The lower apex has radius $r_{\text{tip}} = 10\,\text{nm}$, the total tip length is $L_{\text{tip}} = 10\,\mu\text{m}$, the cone half angle is $\Theta = 10°$, and the bottom point of the tip has the coordinates $[x_c, y_c, d_{\text{min}}]$.

For simplicity, the cantilever was not included in the calculation. This might be taken into account by extending the tip–surface region, thus increasing the number of the matrix elements defined by (7.5).

As the first application, we considered a single potential step along the line $y = 0$ in the plane $z = 0$:

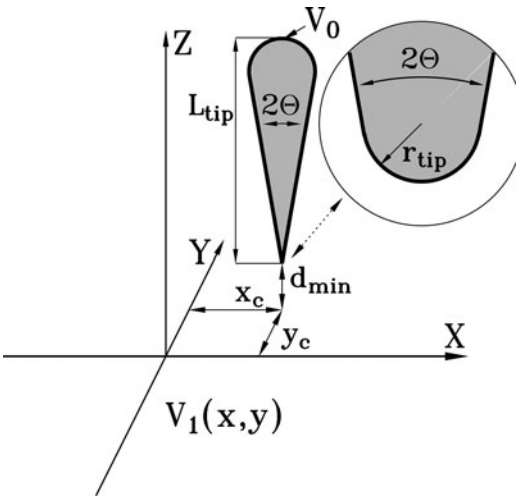

Fig. 7.13 Geometry of the tip–plane system studied in this work, with details of the tip apex geometry shown in the inset. The potential distribution on the plane is marked as $V_1(x, y)$ and the tip surface has the potential V_0. (Reprinted with permission from [55]. Copyright 2007, American Institute of Physics)

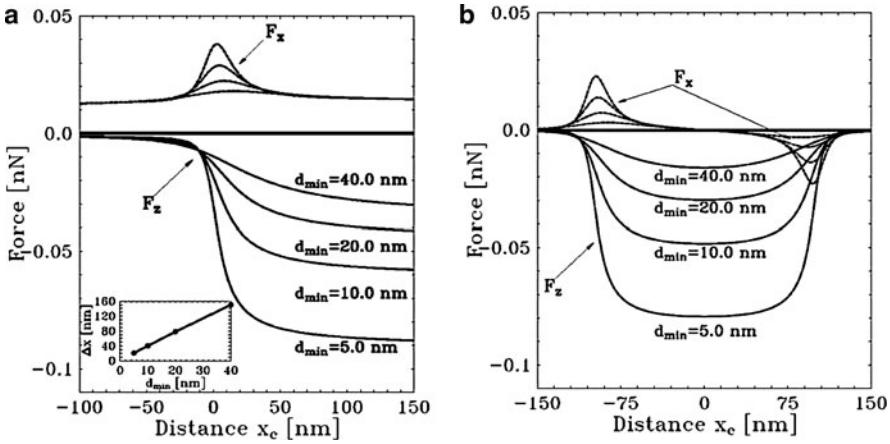

Fig. 7.14 (**a**) Force components F_x and F_z as functions of the x-axis distance x_c between the tip apex and the potential step position, as defined by (7.7). The system considered is shown in Figure 7.13 and is described in the text. F_x values (*dashed lines*) change monotonically with $d_{\min}$, the distance from tip apex to plane. F_x and F_z are of comparable magnitude in the region close to a potential step. (**b**) Force components F_x and F_z as functions of the x-axis distance x_c between the tip apex and the center of the potential island, as defined by (7.9). The system considered is shown in Figure 7.13 and is described in the text. The magnitude of the force components F_x and F_z increases monotonically with decreasing $d_{\min}$ and is of comparable size. (Reprinted with permission from [55]. Copyright 2007, American Institute of Physics)

$$V_1(x, y) = \begin{cases} 0 \text{ for } x < 0, \\ 1 \text{ V for } x > 0. \end{cases} \tag{7.7}$$

The computed force components F_x and F_z are presented in Figure 7.14a ($F_y = 0$ by symmetry).

F_z agrees both qualitatively and quantitatively with the results presented in [57]. As expected, the x-component of the force saturates asymptotically with $F_{-\infty} = 0$ and F_∞ finite, reflecting the potential step. Then, the resolution of the discontinuity determination may be defined in terms of F_z as follows:

$$\Delta x = x_{1-\alpha} - x_\alpha, \tag{7.8}$$

where x_β ($\beta = \alpha$ or $\beta = 1 - \alpha$) are determined from the conditions $F_z(x_\beta) = \beta F_\infty$ [57]. The values of Δx were calculated for $\alpha = 0.25$ and they are presented in the inset of Figure 7.14a, showing a linear dependence on the tip–plane separation, as in [57].

The variation of a lateral force component F_x with x was generally neglected in previous studies [57]. However, the results presented in Figure 7.14a demonstrate that any potential step introduces nonzero lateral components of the electrostatic force, with values not negligible when compared with the vertical component F_z.

This obviously could effect the tip movement and, as a consequence, the physical picture obtained in the experiment. This conclusion is supported by experimental work, where lateral forces were investigated [58] and shown to be important, when the tip approaches a step or an impurity island. These experiments detected lateral forces in the order of 0.05 nN, which is of the same order of magnitude as the values of F_x presented in Figure 7.14a. These results suggest the possibility of determining the position of potential steps using lateral force data, which would complement the method based on F_z values only.

As the second test of the method, a square potential island was considered:

$$V_1(x, y) = \begin{cases} 1\,\mathrm{V} & \text{for } |x| < a/2 \text{ and } |y| < a/2, \\ 0 & \text{elsewhere,} \end{cases} \tag{7.9}$$

with the edge size $a = 200$ nm. Results for the calculated force components, F_x and F_z, are presented in Figure 7.14b.

The function $F_z(x)$ shown in Figure 7.14b tends to zero at large distances, falling to a minimum above the spot. However, for each value of the tip-plane distance $d_{\min}$, the minimum value of F_z does not reach the corresponding saturation level as shown in Figure 7.14a. Therefore, with finite potential islands the magnitude of F_z is smaller and spot-size dependent. Hence, as the island size decreases, the determination of island boundaries from vertical force data becomes more difficult than for step edges.

Now, the following remarks can be made about the values of F_x. There are two potential jumps, at $x = \pm a/2$, and they produce the two peaks of F_x. These peaks, similar to the one presented in Figure 7.14a for the single step, have approximately Lorentzian line shapes and are antisymmetric with respect to $x = 0$, i.e., $F_x = -F_{-x}$, with magnitudes peaking around $x = \pm a/2$. As with the potential step, the peaks in the magnitude of F_x, may be used to estimate the island boundaries. The difference is that, unlike in the case of the potential step, $|F_x|$ decays rapidly to zero for large values of $|x|$.

The last but not least: a numerical advantage of the proposed method is that convergence is achieved with the same number of surface segments for both the potential distributions given by (7.7) and (7.9). This should be compared with numerical force calculations using both the plane and the tip, where typical matrix sizes would be at least an order of magnitude larger.

7.5.3 Numerical Simulation of KPFM Contrast

7.5.3.1 Contact Potential Difference Evaluation

Based on the presented theoretical model of the electrostatic tip–sample interaction we calculated the CPD signal acquired in FM–KPFM. We consider a metallic

tip with potential V_0 placed at a certain height above the surface (x–y plane) and vibrating with the resonant frequency f_0. In the plane, there is a potential distribution $V_1(x, y)$ in the form of one or more islands, each having a fixed value of the electrostatic potential V_i, where $i = 1, 2, \ldots, N$; the rest of the plane has a potential value equal to zero. In such a system, the electrostatic energy W_{el} is given by the formula [56]:

$$W_{\mathrm{el}} = \frac{1}{2} \sum_{i,j=0}^{N} C_{ij} V_i V_j, \tag{7.10}$$

where C_{ij} is a relative capacitance of a pair of conductors i and j. The component F_z of the electrostatic force acting on the tip is given by the expression:

$$F_z \stackrel{\mathrm{def}}{=} -\frac{\partial W_{\mathrm{el}}}{\partial z} = -\frac{1}{2} \sum_{i,j=0}^{N} \frac{\partial C_{ij}}{\partial z} V_i V_j, \tag{7.11}$$

where z is the tip–surface distance. From (7.11) it follows that for fixed potentials V_i ($i = 1, 2, \ldots, N$), F_z is a quadratic function of the tip potential V_0:

$$F_z = \alpha + \beta V_0 + \gamma V_0^2, \tag{7.12}$$

where α, β, and γ are geometry dependent parameters.

In the general case of KPFM, the value of the oscillation amplitude A can be so large that the improved formula for the frequency shift Δf, as derived by the classical perturbation theory [59], has to be used:

$$\frac{\Delta f}{f_0} = -\frac{1}{\pi k A} \int_{-1}^{1} F_z[d_{\min} + A(1 + u)] \frac{u \, \mathrm{d}u}{\sqrt{1 - u^2}}. \tag{7.13}$$

From (7.12) used together with (7.13), it follows that the calculated value of $\Delta f / f_0$ is a quadratic function of V_0, but with modified coefficients α_1, β_1, and γ_1, which result from a corresponding integration of F_z in (7.13). Therefore, the CPD may be written as:

$$\mathrm{CPD} = -\frac{\beta_1}{2\gamma_1}. \tag{7.14}$$

The reviewed general nonlinear method for the CPD evaluation has been used for a direct comparison with the experimental values, as obtained in [40, 41] for KBr islands on the InSb(0 0 1) surface. The results are plotted in Figure 7.15. In the calculations, we used the experimental value of the amplitude of oscillation $A = 40\,\mathrm{nm}$ and fixed the tip–surface distance at $d_{\min} = 1\,\mathrm{nm}$. The only varying paramter was the tip radius, for which we have chosen three values, namely, $r_{\mathrm{tip}} = 5$, 10, and 20 nm.

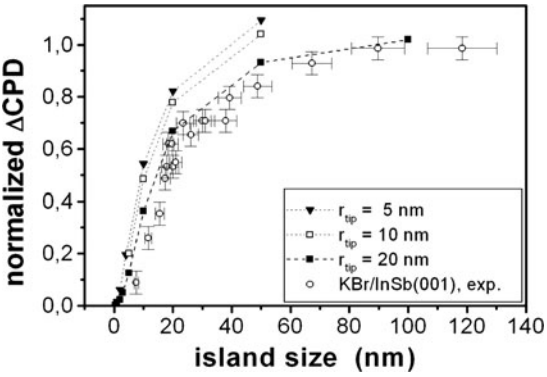

Fig. 7.15 Calculated contact potential difference together with the experimental results for KBr islands on InSb(0 0 1), as a function of the island size. The theoretical results were calculated for fixed values of the vibration amplitude $A = 40\,\text{nm}$, the tip–surface distance $d_{\min} = 1\,\text{nm}$ and $x_c = y_c = 0$, and for three given values of the tip apex radius r_{tip}. The curves between the symbols are guides to eye only

The best agreement between the calculation and experiment is reached if a value of $r_{\text{tip}} = 20\,\text{nm}$ is selected. The results of Figure 7.15 suggest that there might be a possibility of determining the tip geometry parameters from the CPD behavior, when measurement and calculation are performed for a series of island sizes. The results of more detailed calculation of the CPD for different surface potential distributions (potential islands) have been presented in [60], to which we refer the interested reader for complete details.

7.6 High Resolution KPFM Measurements

7.6.1 Limits of Lateral Resolution in FM–KPFM

Once we have discussed the capability of FM–KPFM to map the true values of the surface potential, the second question arises, concerning the observed lateral resolution of the CPD contrast in the sub-nanometer scale as it has been recently reported in a few experiments [61–64]. The atomic contrast in the CPD signal is an evidence that some short-range electrostatic forces are probed with KPFM. To explore in more detail the issue for which interactions are detected by the KPFM, we have performed FM–KPFM imaging of nanostructures formed during the deposition of gold on semiconductor surfaces. Figure 7.16 shows the topography (a) and CPD images (b) of Au grown on InSb(0 0 1), respectively. For the experimental conditions used, gold grows predominantly in the form of rectangular islands with a typical height of a few monolayers of Au (about 2.0 nm), and there is a certain amount of material spread over the substrate surface (i.e., between the islands).

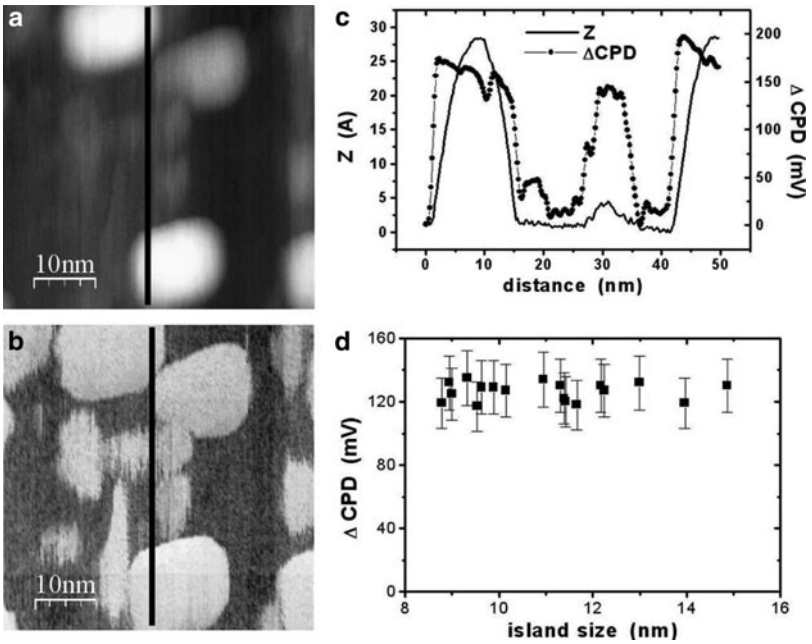

Fig. 7.16 (**a**) FM–KPFM topography and (**b**) corresponding CPD map of 0.2 ML Au grown on a InSb(0 0 1) surface at 400 K ($f_0 = 249.0$ kHz, $\Delta f = -6$ Hz). (**c**) topography (*solid line*) and CPD (*solid circles*) profiles taken along the lines on images (**a**) and (**b**). (**d**) Measured CPD versus lateral size of the 2 nm high Au islands

From the comparison between the topography and CPD images it follows that the CPD map provides more details concerning the developed surface topography. Some small features, which are difficult to recognize in the topography image, due to a large variation of the image in the z-direction, are easily recognized with the help of CPD signal. Moreover, almost the same CPD contrast, for Au islands and spread material, indicates that they are of the same chemical composition. Thus, KPFM is able to give information about the chemical composition of the surface, provided there is some reference marker on the imaged surface, i.e., the Au islands in this study. The gold topography features show a higher surface potential in comparison with the substrate surface, according to what is generally expected due to the higher work function of gold with respect to a clean InSb surface. However, despite a large difference in the amount of material constituting both the islands and the features seen between the islands as well as the difference in their lateral dimensions, both kind of structures exhibit almost the same CPD. This is in contrast to the observed dependence of the work function on Au film coverage. For example, for the Au/W(0 0 1) system [12], the measured work function saturates at a value corresponding to the one of bulk Au, at the least coverage of 3 ML Au.

Figure 7.16c presents topography (solid line) and CPD (solid circles) line profiles along the lines shown in the two 2D images in Figure 7.16a, b. The profiles depict

that the areas of increased CPD correspond to the areas of the topographic features at their bases. The CPD signal changes simultaneously with the topographic one, but the CPD profile is steeper. The CPD signal reaches its saturation levels, in both uphill and downhill direction of the islands, much faster than the topography signal. Since in KPFM the topography image is due to the van der Waals and chemical interactions between the tip and the sample, with the relative contribution depending on the actual tip–apex shape, one can draw two conclusions. First, the observed changes of the CPD signal, faster than the topography ones, indicate that the Kelvin controller for surface potential compensation probes interactions which have the interaction range shorter than that of the van der Waals interaction. Second, the weak dependence of the CPD on the volume of the imaged Au features indicates that the interaction is limited to the tip apex and the closest single surface gold atoms. These conclusions are further supported by the observed lack of the dependence of the CPD on the Au island size. As Figure 7.16d clearly demonstrates, the FM–KPFM measurements of the 2.0 nm thick Au islands of lateral edge sizes ranging from 8 up to 15 nm, resulted in almost the same CPD, whereas for the KBr/InSb system such a change of the KBr island size was reflected in a change of the CPD by a factor of 2 (see Fig. 7.12).

7.6.2 Characterization of the Short-Range Bias Dependent Interactions: Quasispectroscopic KPFM Measurements

In order to evaluate the range of interaction contributing to the observed "high quality" of the CPD (as seen in Fig. 7.16b), we have performed "quasi-spectroscopic" measurements for the Au/InSb(0 0 1) system. We have found that for certain growth conditions on the InSb(0 0 1) surface, gold organizes itself in form of flat and elongated islands (nanowires) of about 1 nm height and a few hundreds nanometers length. Therefore, this system provides a good template for performing the required quasi-spectroscopic FM–KPFM measurements as described below.

When using SPM at room temperature, it is usually difficult to perform reliable spectroscopy measurements over a specific surface site, since the thermal drift and/or piezoscanner creep give large uncertainty, both for "in-plane" tip position, as well as in its height determination. To overcome this problem, we have performed FM–KPFM measurements of the Au nanowires grown on the InSb(0 0 1) surface in two distinct regimes of the imaging. In the first regime, we could acquire a clear topography image of the Au islands with corresponding sharp CPD contrast, while in the other regime, the same Au islands can still be seen in the topography but can be hardly resolved in the corresponding CPD map. The former conditions correspond to imaging with relatively large detuning, in this case $\Delta f = -15\,\mathrm{Hz}$ (tip "close" to the surface), whereas the latter ones correspond to imaging with a much smaller detuning of $\Delta f = -3\,\mathrm{Hz}$ (the tip retracted from the surface). The system was stable and we could repeat this kind of imaging several times. The

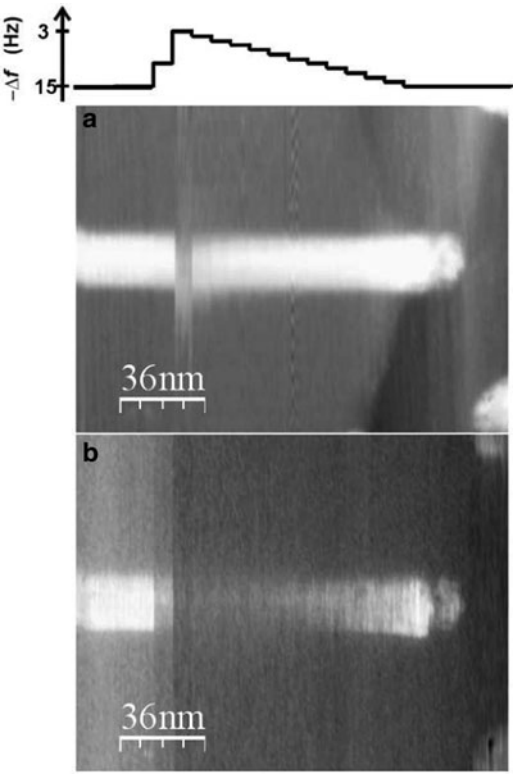

Fig. 7.17 (**a**) FM–KPFM topography and (**b**) corresponding CPD map of a Au island (nanowire) grown on a InSb(0 0 1) surface at 560 K ($f_0 = 358.4$ kHz). Above the image a schematic of the changes of the detuning magnitude during the acquisition of the images is shown. For better visualization of the apparent change of the island height the topography image was flattened with a line-by-line subtraction of an offset line in the fast scan direction. Reprinted with permission from [64]

imaging was performed with the fast scan direction being always perpendicular to the nanowire. Then, a sample surface with relatively low density of islands has been chosen to obtain in the AFM image frame that has only a single Au nanowire. While imaging the nanowire, after acquisition of every few tens of scan lines, the detuning was gradually changed by 1 Hz between the two distinguished values of Δf, namely, -15 and -3 Hz. The results are shown in Figure 7.17a, b (topography and CPD maps), respectively, with the corresponding scheme of the detuning changes. From the cross section of the topography image taken along the slow scan direction, the tip–surface separation changes have been extracted and attributed to the corresponding changes of the detuning.

Next, from the cross sections taken along the fast scan direction, the apparent island height and corresponding CPD for a given detuning have been evaluated. Having calibrated the tip–surface distance change versus the detuning change, the dependences of the island height and the CPD on the relative tip-surface separation change were obtained, as shown in Figure 7.18. The zero value in the abscissa axis corresponds to the closest distance between the tip and the sample ($\Delta f = -15$ Hz).

The decreasing of the detuning down to $\Delta f = -3$ Hz resulted in the increase of the tip–surface separation by 2.2 nm. The apparent island height exhibits a slow

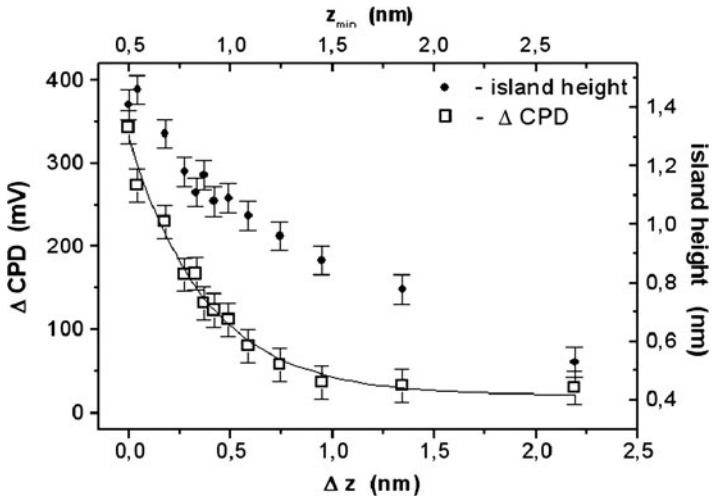

Fig. 7.18 Dependences of the apparent Au island height and corresponding CPD on the tip–surface separation change. The upper abscissa axis, $z_{\min}$, is the evaluated distance of the closest tip–surface approach. The data were extracted from the quasispectroscopic measurements presented in Fig. 7.17. Reprinted with permission from [64]

decrease as the tip is retracted from the surface, whereas the CPD exhibits a faster exponential-like decay dependence on the tip–sample separation. The exponential fit CPD $\sim \exp(-\Delta z/\lambda)$ reveals the decay length of the CPD signal of $\lambda = 0.38$ nm. The faster disappearance of the CPD signal than the topography contrast as the tip is retracted from the surface indicates that the interactions contributing to the measured CPD are of shorter range than the van der Waals ones. The observed saturation of the CPD signal on the level of about 30 mV at higher tip–surface separation we associate with the contribution of the "true" CPD due to the long range electrostatic interactions between the tip and the Au island. We have evaluated the distance between the surface and the tip apex at its turning point (the closest approach) of the oscillation cycle, $z_{\min}$, taking into account van der Waals interactions only. We have considered the following expression for the corresponding frequency shift derived for the van der Waals interaction between a sphere of radius R and infinite plane [65]:

$$\Delta f_{\mathrm{VdW}}/f_0 = -\frac{HR}{12kAz_{\min}(2z_{\min}A)^{1/2}}, \tag{7.15}$$

where we used the experimental values of the cantilever spring constant $k = 20\,\mathrm{N\,m^{-1}}$, the Hamaker constant [66] $H = 8 \times 10^{-21}$ J, $R = 20$ nm and the oscillation amplitude $A = 20$ nm. From these data, we have evaluated the closest approach of the tip to the surface at the $\Delta f = -3$ Hz as $z_{\min} = 2.7$ nm (Fig. 7.18).

The results presented provide the experimental evidence that in the FM–KPFM technique some short-range, bias-dependent interactions between the tip and the

surface may be detected. These interactions eventually contribute to the observed "high quality" CPD contrast. A rough estimate of the tip–sample separation during the imaging of the Au/InSb(0 0 1) system indicates that the interactions are detected when the tip–surface separation is of the order of 1 nm or smaller. For the tip being "far enough" from the surface, only long-range electrostatic interactions are bias-dependent. In this case, FM–KPFM provides the CPD signal related to the surface potential distribution on the sample and the measured CPD contrast depends on the experimental conditions, such as the ratio of the tip and surface structure dimensions. This is demonstrated for the KBr/InSb(0 0 1) system, where the measured CPD contrast depends on the KBr island size. This observation is then supported by the predictions of the theoretical model presented in Sect. 7.5.2.1, which takes into account only long-range electrostatic interactions between the tip and the surface.

When some other bias-dependent interactions between the tip and the surface are active, the interpretation of the experimental CPD contrast is more complicated. In this case, the measured CPD signal does not reflect the voltage which compensates the CPD between the tip and the sample. Rather, it corresponds to the voltage for which the sum of the long-range electrostatic interaction (due to the CPD between the tip and the sample) and the short-range interactions (related to the front tip atom and surface) has its minimum. In particular, the measured CPD signal does not reflect the distribution of the work function on the imaged surface.

7.7 Summary

In this chapter we have presented the surface properties, related to nanostructures supported on semiconductor substrates. The main part of the experimental results, presented above, was obtained by KPFM in UHV. The investigated systems include:

- Epitaxial nanostructures assembled on InSb(0 0 1) by submonolayer deposition of Au.
- Semiconductor nanostructures grown on lattice-mismatched semiconductor substrates.
- Semiconductor surfaces with surface modification and nanostructuring induced by ionizing irradiation.
- Dielectric structures grown on InSb(0 0 1).

We have also presented a new efficient algorithm for evaluation of electrostatic forces in the tip–plane system. Based on this method, we calculated the CPD values for the considered tip–plane systems and compared the theoretical results with the experimental data. We have presented these results, which show a good agreement with the experiment.

In the last part of the chapter, we have analyzed and discussed the important issue of high resolution measurements. Particularly, using the Au/InSb(001) system as an

example, we have addressed the key problem of the limits of lateral resolution. Then, the subject of the quasispectroscopic KPFM measurements has been discussed. Finally, we have discussed the phenomenon of the so-called short-range bias-dependent electrostatic interactions.

Acknowledgements This work was supported by the Polish Ministry of Science and Higher Education within the framework of program of European Science Foundation, ESF, EUROCORE – FANAS, project Active Control of Friction, ACOF. We thank M. Goryl and K. Sajewicz for providing the images from their work, and P. Piatkowski for helping in the upgrade of VP2 system.

References

1. M. Tomitori, T. Arai, Appl. Surf. Sci. **140**, 432 (1999)
2. C. Joachim, J.K. Gimzewski, A. Aviram, Nature **408**, 541 (2000)
3. M. Szymonski, M. Goryl, F. Krok, J.J. Kolodziej, F. Buatier de Mongeot, Nanotechnology **18**, 044016 (2007)
4. M. Goryl, J.J. Kolodziej, F. Krok, P. Piatkowski, B. Such, M. Szymonski, Microelectron. Eng. **81**, 394 (2005)
5. J.J. Kolodziej, B. Such, M. Szymonski, F. Krok, Phys. Rev. Lett. **90**, 226101 (2003)
6. M.O. Schweitzer, T.S. Jones, C.F. McConville, N.V. Richardson, Surf. Sci. **287-288**, 545 (1993)
7. P.J. Feibelman, D.R. Hamann, Phys. Rev. B **29**, 6463 (1984)
8. G.W. Gobeli, F.G. Allen, Phys. Rev. **137**, 245 (1965)
9. G. Goryl - PhD thesis, Jagiellonian University 2011
10. Y. Shapira, F.Xu, D.M. Hill, J.H. Weaver, Appl. Phys. Lett. **51**, 118 (1987)
11. M. Goryl, F. Krok, J.J. Kolodziej, P. Piatkowski, B. Such, M. Szymonski, Vacuum **74**, 223 (2004)
12. G.W. Graham, Phys. Rev. B **32**, 2640 (1985)
13. H. Wagner, in *Solid Surface Physics: Physical and Chemical Properties of Stepped Surfaces*, vol. 85 of Springer Tracts in Modern Physics (Springer, Berlin, 1979)
14. H. Ibach, W. Schmickler, Phys. Rev. Lett. **91**, 016106 (2003)
15. R. Smoluchowski, Phys. Rev. **60**, 661 (1941)
16. H. Sakaki, Solid State Commun. **92**, 119 (1994)
17. D. Leonard, M. Krishnamurthy, C.M. Reaves, S.P. Denbaars, P.M. Petroff, Appl. Phys. Lett. **63**, 3203 (1993)
18. J.-Y. Marzin, J.-M. Gerard, A. Izrael, D. Barrier, G. Bastard, Phys. Rev. Lett. **73**, 716 (1994)
19. B.J. Hinds, T. Yamanaka, S. Oda, J. Appl. Phys. **90**, 6402 (2001)
20. K. Hishiguchi, X. Zhao, S. Oda, J. Appl. Phys. **92**, 2748 (2002)
21. K. Arai, S. Oda, Phys. Status Solidi C **0**, 1254 (2003)
22. M.A. Salem, H. Mizuta, S. Oda, Appl. Phys. Lett. **85**, 3262 (2004)
23. T. Yamauchi, M. Tabuchi, A. Nakamura, Appl. Phys. Lett. **84**, 3834 (2004)
24. T. Yamauchi, Y. Ohyama, Y. Matsuba, M. Tabuchi, A. Nakamura, Appl. Phys. Lett. **79**, 2465 (2001)
25. A. Yabe, H. Niino, in *Laser Ablation of Electronic Materials*, ed. by E. Fogarassy, S. Lazare (Elsevier, Amsterdam, 1992), p. 199
26. W.L. Chan, E. Chason, J. Appl. Phys. **101**, 121301 (2007)
27. J. Reif, F. Costache, M. Bestehorn, in *Recent Advances in Laser Processing of Materials*, ed. by J. Perrier, E. Millon, E. Fogarassy (Elsevier, Amsterdam, 2006) p. 275
28. M.A. Makeev, R. Cuerno, A.-L. Barabasi, Nucl. Instrum. Meth. B **197**, 185 (2002)
29. Z. Guosheng, P.M. Fauchet, A.E. Siegman, Phys. Rev. B **26**, 5366 (1982)

30. J. Reif, M. Ratzke, O. Varlamova, F. Costache, Mater. Sci. Eng. B **134**, 114 (2006)
31. S. Facsko, T. Dekorsy, C. Koerdt, C. Trappe, H. Kurz, A. Vogt, H.L. Hartnagel, Science **285**, 1551 (1999)
32. C.M. Demanet, J.B. Malherbe, N.G. van der Berg, V. Sankar, Surf. Interf. Anal. **23**, 433 (1995)
33. F. Krok, Vacuum **83**, 745 (2008)
34. P. Sigmund, Phys. Rev. **184**, 383 (1969)
35. J. Massies, L. Dazaly, J. Appl. Phys. **55**, 3136 (1984)
36. M. Bouslama, C. Jardin, M. Ghamnia, Vacuum **46**, 143 (1995)
37. F. Krok, J.J. Kolodziej, B. Such, P. Piatkowski, M. Szymonski, Appl. Surf. Sci. **210**, 112 (2003)
38. M. Szymonski, F. Krok, P. Struski, J. Kolodziej, B. Such, Progress in Surf. Sci. **74**, 331 (2003)
39. Ch. Sommerhalter, Th.W. Matthes, Th. Glatzel, A. Jaeger-Waldau, Appl. Phys. Lett. **75**, 286 (1999)
40. J.J. Kolodziej, B. Such, P. Czuba, F. Krok, P. Piatkowski, M. Szymonski, Surf. Sci. **506**, 12 (2002)
41. F. Krok, P. Piatkowski, J.J. Kolodziej, B. Such, P. Struski, P. Czuba, M. Szymonski, Surf. Science **566–568**, 63 (2004)
42. S. Sadewasser, M. Ch. Lux-Steiner, Phys. Rev. Lett. **91**, 266101 (2003)
43. B. Such, F. Krok, M. Szymonski, in *Scanning Force Microscopies for Imaging and Characterisation of Nanostructured Materials*, ed. by A. Korkin, E. Gusev, J.K. Labanowski, S. Luryi. Nanotechnology for Electronic Materials and Devices (Springer, Berlin 2007)
44. Y. Rosenwaks, R. Shikler, Th. Glatzel, S. Sadewasser, Phys. Rev. B **70**, 085320 (2004)
45. U. Zerweck, Ch. Loppacher, T. Otto, S. Grafstrom, L.M. Eng, Phys. Rev. B **71**, 125424 (2005)
46. L.N. Kantorovich, A.S. Foster, A.L. Shluger, A.M. Stoneham, Surf. Sci. **445**, 283 (2000)
47. G. Mesa, E. Dobado-Fuentes, J.J. Sáenz, J. Appl. Phys. **79**, 39 (1996)
48. G. Mesa, J.J. Sáenz, Appl. Phys. Lett. **68**, 1169 (1996)
49. S. Gómez-Monivas, L.S. Froufe-Pérez, A.J. Caamano, J.J. Sáenz, Appl. Phys. Lett. **79**, 4048 (2001)
50. S. Watanabe, K. Hane, T. Ohye, M. Ito, T. Goto, J. Vac. Sci. Technol. **11**, 1774 (1993)
51. H.O. Jacobs, H.F. Knapp, S. Müller, A. Stemmer, Ultramicroscopy **69**, 39 (1997)
52. H.O. Jacobs, P. Leuchtmann, O.J. Homan, A. Stemmer, J. Appl. Phys. **84**, 1168 (1998)
53. A. Gil, J. Colchero, J. Gómez-Herrero, A.M. Baró, Nanotechnology **14**, 332 (2003)
54. S. Hudlet, M. Saint Jean, C. Guthmann, J. Berger, Eur. Phys. J. **2**, 5 (1998)
55. J. Konior, J. Appl. Phys. **101**, 084907 (2007)
56. J.D. Jackson, *Classical Electrodynamics* (Wiley, New York, 1998)
57. S. Belaidi, F. Lebon, P. Girard, G. Leveque, S. Pagano, Appl. Phys. A **66**, S239 (1998)
58. O. Pfeiffer, R. Bennewitz, A. Baratoff, E. Meyer, Phys. Rev. B **65**, 161403 (2002)
59. F. J. Giessibl, Phys. Rev. B, **56**, 24 (1997)
60. K. Sajewicz, F. Krok, J. Konior, Jap. J. Appl. Phys. **49**, 025210 (2010)
61. Y. Sugawara, T. Uchihashi, M. Abe, S. Morita, Appl. Surf. Sci. **140**, 371 (1999)
62. S. Kitamura, K. Suzuki, M. Iwatsuki, C. Mooney, Appl. Surf. Sci. **157**, 222 (2000)
63. K. Okamoto, K. Yoshimoto, Y. Sugawara, S. Morita, Appl. Surf. Sci. **210**, 128 (2003)
64. F. Krok, K. Sajewicz, J. Konior, M. Goryl, P. Piatkowski, M. Szymonski, Phys. Rev. B **77**, 235427 (2008)
65. M. Guggisberg, M. Bammerlin, Ch. Loppacher, O. Pfeiffer, A. Abdurixit, V. Barwich, R. Bennewitz, A. Baratoff, E. Meyer, H.-J. Guntherodt, Phys. Rev. B **61**, 11151 (2000)
66. L. Bergstrom, Adv. Colloid Interface Sci. **70**, 125 (1997)